High-Resolution Imaging of Hydraulic-Fracturing-Induced Earthquake Clusters in the Dawson-Septimus Area, Northeast British Columbia, Canada

Marco P. Roth[*1], Alessandro Verdecchia[1,2], Rebecca M. Harrington[1], and Yajing Liu[2]

Abstract

The number of earthquakes in the western Canada sedimentary basin (WCSB) has increased drastically in the last decade related to unconventional energy production. The majority of reported earthquakes are correlated spatially and temporally with hydraulic fracturing (HF) well stimulation. In this study, we use waveform data from a new deployment of 15 broadband seismic stations in a spatial area of roughly 60×70 km^2, covering parts of the Montney Formation, to study the relationship between earthquakes and HF operations in the Dawson-Septimus area, British Columbia, Canada, where the two largest HF-related earthquakes in WCSB to date, an M_w 4.6 on 17 August 2015 and an M_L 4.5 on 30 November 2018, have occurred. We use an automated short-term average/long-term average algorithm and the SeisComP3-software to detect and locate 5757 local earthquakes between 1 July 2017 and 30 April 2019. Using two clustering techniques and double-difference relocations of the initial catalog, we define event families that are spatially associated with specific wells, and exhibit temporal migration along a horizontal well bore and/or multiple fractures close to wells. Relocated clusters align in two dominant orientations: one roughly perpendicular to the maximum horizontal regional stress direction (S_H) and several conjugate structures at low angles to S_H. Comparing the two predominant seismicity lineations to regional earthquake focal mechanisms suggests that deformation occurs via thrust faulting with fault strike oriented perpendicular to S_H and via strike-slip faulting with strike azimuth at low angles to S_H. Local scale seismicity patterns exhibit clustering around individual HF wells, whereas regional scale patterns form lineations consistent with deformation on faults optimally oriented in the regional stress field.
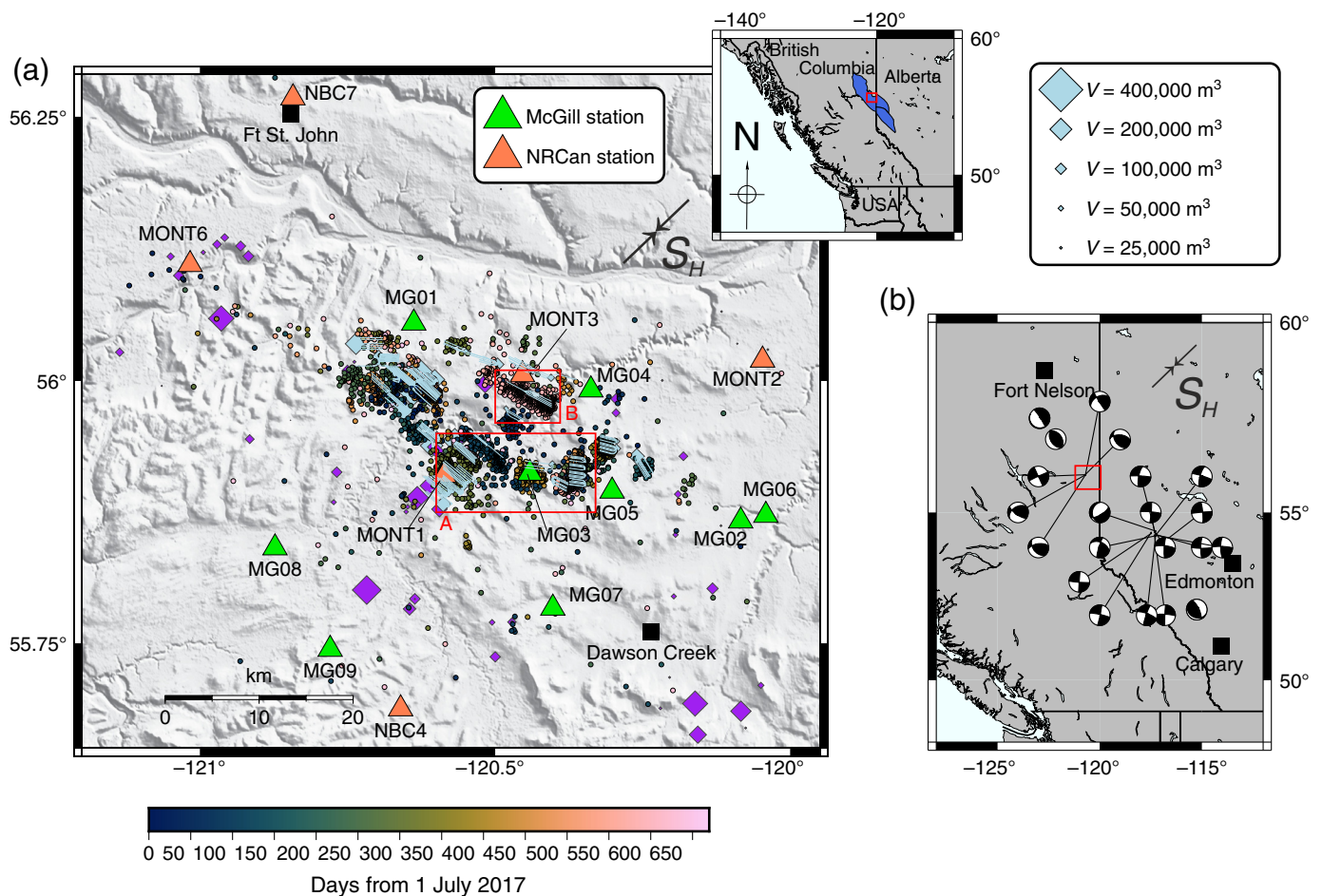
Introduction

The proliferation of hydraulic-fracturing (HF)-based fluid injection operations related to unconventional energy production has ushered in a large number of earthquakes in some parts of North America with historically low-seismicity rates (e.g., Ellsworth, 2013; Atkinson *et al.*, 2016). Although induced earthquakes in the central United States are often attributed to the disposal of coproduced wastewater from HF activity injected at low pressures over long periods of time, induced earthquakes in the western Canada sedimentary basin (WCSB) are often associated with HF injection itself (Atkinson *et al.*, 2016; Bao and Eaton, 2016; Babaie Mahani *et al.*, 2017; Ghofrani *et al.*, 2019). Injection related to HF entails volumes that are often an order of magnitude less than those associated with wastewater disposal, albeit at much

higher pressures. Thus, the majority of induced events that occur directly from HF injection are often small-magnitude events that cause shaking below the threshold commonly felt by the surrounding population (Ellsworth, 2013). Nevertheless, an increasing number of exceptions of damaging HF-induced earthquakes have recently occurred, including an M_w 4.7 on 28 January 2017 and an M_L 5.7 on 3 January 2019 in the Sichuan basin, China (Lei *et al.*, 2017, 2019), as well as a number of M_w 3+ earthquakes in the WCSB.

1. Ruhr University Bochum, Bochum, Germany; 2. McGill University, Montréal, Québec, Canada

*Corresponding author: marco.roth@rub.de

Figure 1. (a) Overview map of the Dawson-Septimus area. Green and orange triangles denote stations maintained by McGill University and Pacific Geoscience Centre, respectively. Colored circles show the epicenters of earthquakes in the database between 1 July 2017 and 30 April 2019, with origin time indicated by the colorbar. Turquoise diamonds denote hydraulic fracturing (HF) wells active in the catalog time period, whereas purple diamonds denote those with no correlated seismicity. The red boxes A and B highlight the areas for Figures 6 and 7, respectively. The small inset map shows the location of our study area (red box) and the shape of the Montney Formation as reported by the British Columbia Oil and Gas Commission (BCOGC) and Alberta Energy Regulator. (b) Map of focal mechanism solutions of M_w 3+ earthquakes by other studies (see the Introduction) in the western Canada sedimentary basin. Focal mechanism plots in the study area of this work contain events of smaller magnitudes. NRCan, Natural Resources Canada. The color version of this figure is available only in the electronic edition.

The Montney Formation is located in northeast British Columbia and is the largest unconventional shale gas play within the WCSB with nearly 3000 production wells (British Columbia Oil and Gas Commission [BCOGC], 2017). Production activity in the low-permeability tight shale developed rapidly starting in 2005, and has been accompanied by an increasing number of M_w 3+ earthquakes (Atkinson et al., 2016). In fact, the Montney Formation has hosted the largest HF-induced earthquakes in Canada to date, including an M_w 4.6 on 17 August 2015 near Fort St. John (Babaie Mahani et al., 2017; Wang et al., 2020) and an M_L 4.5 on 30 November 2018 near Dawson Creek (Babaie Mahani et al., 2019; Peña-Castro et al., 2020). The increased number and the range of earthquake magnitudes produced due to HF injection activity in the WCSB highlight the importance of two primary factors that should be considered in estimating the hazard associated with induced events: the influence of pre-existing faults or zones of weakness and the relation between injection parameters in earthquake timing and magnitude (McGarr et al., 2015).

Here, we present a new earthquake catalog from a dense deployment of stations near Dawson Creek, British Columbia, within 50 km of the epicenter of the M_L 4.5 on 30 November 2018, with data collection starting in July 2017 (Fig. 1a). Our study combines the spatial and temporal relationship between earthquakes and stimulation parameters reported by the BCOGC (see Data and Resources) and uses double-difference earthquake relocations as well as focal mechanism solutions from other studies to infer the dominant orientation of geological structures activated by HF injection (Eaton and Babaie Mahani, 2015; Schultz, Mei, et al., 2015; Zhang et al., 2016;

Babaie Mahani *et al.*, 2017; Schultz *et al.*, 2017; Wang *et al.*, 2018; Peña-Castro *et al.*, 2020; see Fig. 1b) to infer geological structures activated by injection. We also apply two clustering algorithms and use reported injection data to show individual families correlate with individual HF injection phases, and exhibit temporal migration within families.

In the following, we first present the automated earthquake catalog building procedure and the clustering methods, followed by the earthquake relative relocation results as well as fault structural interpretations. We will show a strong correlation between seismicity and HF stimulation and a distribution of possible pre-existing structures that were reactivated to produce some of the recent slip events in the WCSB, in spite of small reported injection volumes related to HF.

Earthquake Catalog Building

To build the detailed earthquake catalog for the study area shown in Figure 1, we use new data from an array of 15 broadband stations spaced in an area of roughly 60×70 km^2 in the Dawson-Septimus area, British Columbia. The time period of data collection ranges from 1 July 2017 to 30 April 2019. Of the 15 stations, nine are part of the XL network operated by McGill University, four are part of the 1E network, and two are part of the (permanent) CN network; the latter two networks are both operated by Pacific Geoscience Centre of the Geological Survey of Canada (Fig. 1, Data and Resources). A complete list of latitude and longitude coordinates and station names appears in Table S1 (available in the supplemental material to this article).

We use the software SeisComP3 (Weber *et al.*, 2007) to detect and locate earthquakes in an automated fashion, in which each automated detection is manually reviewed by an analyst to improve phase pick, and corresponding location accuracy. A short-term average/long-term average (STA/LTA) trigger detects *P*-wave first arrivals, in which the best settings were empirically determined using a test data set in a time period from 12 July 2017 to 31 August 2017. Parameter settings include a 3–20 Hz, fourth-order Butterworth band-pass filter, an STA duration of 0.2 s, LTA duration of 10 s, a triggering threshold of 2.5, and a detriggering threshold of 1.5. We apply a 3–12 Hz, third-order Butterworth band-pass filter and an Akaike information criterion algorithm to detect *S*-wave first arrivals. Applying the earlier settings on the test data set from 12 July 2017 to 31 August 2017 (roughly 1.5 months) yields 491 detections, of which we determine by visual inspection that 128 are false detections. We then apply the earlier settings on the entire data set that spans a 21.5-month time period.

As mentioned previously, following the event detection, an analyst reviews both the *P*- and *S*-phase pick accuracy and corrects the automated pick if necessary. We then use the open-source program NonLinLoc (Lomax *et al.*, 2000) combined with a local velocity model based on Crust1.0 (Laske *et al.*, 2013; Babaie Mahani *et al.*, 2017), to calculate event locations. The hybrid velocity model uses the Crust1.0 (Laske *et al.*, 2013)

model for depths shallower than 1 km, and the Babaie Mahani *et al.* (2017) model for greater depths (Fig. S1). After finalizing the earthquake hypocenter estimations, we determine the local magnitude with a relation specified for WCSB (Yenier, 2017) based on the peak-to-peak amplitude of the horizontal components of the Wood–Anderson waveform. To consider the location error ensuing from the 1D horizontal-layered velocity model, we are listing only events with a horizontal error smaller than 3 km into this initial automated catalog.

The catalog building settings determined earlier for the test data set result in a total of 5757 earthquakes with magnitudes ranging from −0.6 to 4.5 for the entire study period, excluding false detections (removed by visual inspection), inferred quarry blasts located southwest of the study area, and teleseismic events. Of the 5757 earthquakes referenced previously, we impose a quality control criterion requiring horizontal error smaller than 3 km, estimated from the resulting location error of latitude and longitude, before listing events in the catalog. Imposing the quality control criteria reduces the number of cataloged events to 4883 (Fig. 1). We also estimate the catalog completeness M_c at 1.3, and the Gutenberg–Richter *b*-value at 0.92 using a maximum-likelihood estimate (Aki, 1965; Wiemer and Wyss, 2000; Fig. S2). The details of the Gutenberg–Richter relation and statistical parameter estimation can be found in Figure S2.

Figure 1 shows the spatial distribution of the 4883 events from the initial catalog between 1 July 2017 and 30 April 2019, as well as HF wells that were stimulated in the same time period. On a regional scale, seismicity lineations follow a northwest–southeast-striking trend, that is, perpendicular to S_H and parallel to S_h according to the regional stress regime (Bell and Grasby, 2012). The majority of events occur in close proximity to HF wells, operating in the same time period, whereas one can observe operating wells in the southwestern part of the study area without a large number of events close by, in spite of the non-negligible injection volumes. The largest event, the M_L 4.5, is located close to MG01 (Fig. 1) at a well with a moderate amount of injected volume (Peña-Castro *et al.*, 2020). Thus, we do not observe a clear correlation between magnitude and injected volume in this area.

After building the initial earthquake catalog, we examine the timing of events and the correlation with well stimulation. We start by binning earthquakes in the entire study region (i.e., the entire catalog described earlier) in 24 hr bins to identify temporal periods with elevated seismicity, as well as establish potential fluctuations in background seismicity. The resulting histogram reveals temporal clusters of events that closely associate with reported stimulation activity and provides a starting point for using enhanced clustering methods to investigate the relationship between seismicity and HF stimulation.

Figure 2 shows the temporal distribution of earthquakes in the catalog during the time period detailed previously as black bars and highlights distinctive periods for which seismic
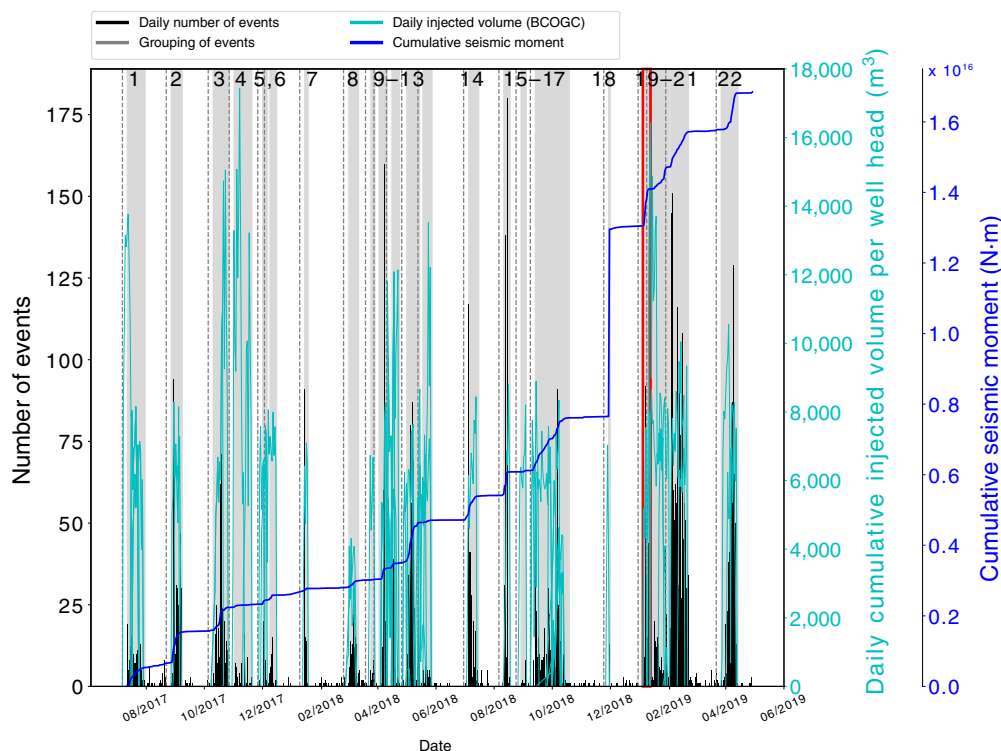
Figure 2. Temporal distribution of cataloged earthquakes over the study period. Black bars show the daily number of earthquakes; the blue line shows the cumulative seismic moment. The gray-shaded areas denote the temporal windows of elevated seismicity in which four or more events happened on successive days. Marked in red is the time window 19, in which we highlight the earthquake–HF stage coupling in more detail in Figure 8. Starting time of temporal windows includes a five-day buffer prior to the gray-shaded area. Turquoise lines indicate the cumulative daily injected fluid volume per well head for all wells within 5 km of the groups of earthquakes families active in the time window (see the Earthquake Catalog Building section). The color version of this figure is available only in the electronic edition.

curve in the figure demonstrates the strong correlation between earthquake occurrence and nearby HF operations, and provides the basis for the qualitative temporal grouping of earthquakes in the gray-shaded areas.

Event Spatiotemporal Clustering

An initial assessment of Figure 2 suggests earthquakes occur primarily in 22 temporal groups. We use the 22 temporal groups to perform a spatial clustering analysis that will be used as a basis to define individual event families for cluster-based event double-difference relocation (to be described in the Seismicity Relocation section). We use two clustering methods: (1) a network similarity matrix (Grund *et al.*, 2016) approach based on common features in event waveforms, and (2) a statistical approach based on the time–space–energy domain (Zaliapin *et al.*, 2008). The network similarity matrix independently assesses the spatial clustering of events from the temporal clustering suggested by the histogram, whereas the time–space–energy domain considers spatial and temporal grouping simultaneously. We will show later that both clustering algorithms suggest the events are highly spatially clustered around HF wells.

activity is high. The figure also depicts quiescent periods for which the daily number of events is low. We initially define temporal groups of seismicity by time windows for which four or more earthquakes occurred on consecutive days, with a buffer of five days placed before the start of the time window. Gray-shaded areas indicate time windows with consecutive days of earthquakes, along with the five-day buffer shown as vertical gray dashed lines in Figure 2. The dark blue curve describes the cumulative seismic moment of the earthquakes shown in the histogram, in which steps in the curve also highlight where seismic activity is temporally clustered (in addition to gray-shaded areas), as opposed to a steady accumulation of moment through the occurrence of background events. Figure 2 also shows the cumulative volume of injected fluid during HF operations as turquoise lines for the wells spatially associated with earthquakes, which are indicated by the light blue diamonds in Figure 1. Cumulative injection volume data for wells located outside the area of vigorous earthquake activity, seen as purple diamonds in Figure 1, are not plotted in Figure 2. A comparison of the black bars and the turquoise

The network similarity matrix approach is based on waveform similarity between events observed across a network of seismic stations and uses a set of matrix cross-correlation coefficients (CCCs) calculated at the individual network stations as indicators of event proximity. One advantage to using the network approach is that combining CCCs from multiple stations into a single similarity matrix can remove dependencies on temporal station-related restrictions, such as hardware problems or periods of increased noise. It works by first calculating the CCC on each station component individually for a given event pair, and uses the signal-to-noise ratio (SNR) at each station as a weighting factor before combining the station CCCs into a common matrix (Grund *et al.*, 2016). The CCCs that are used as input variables into the matrix are, in general, not
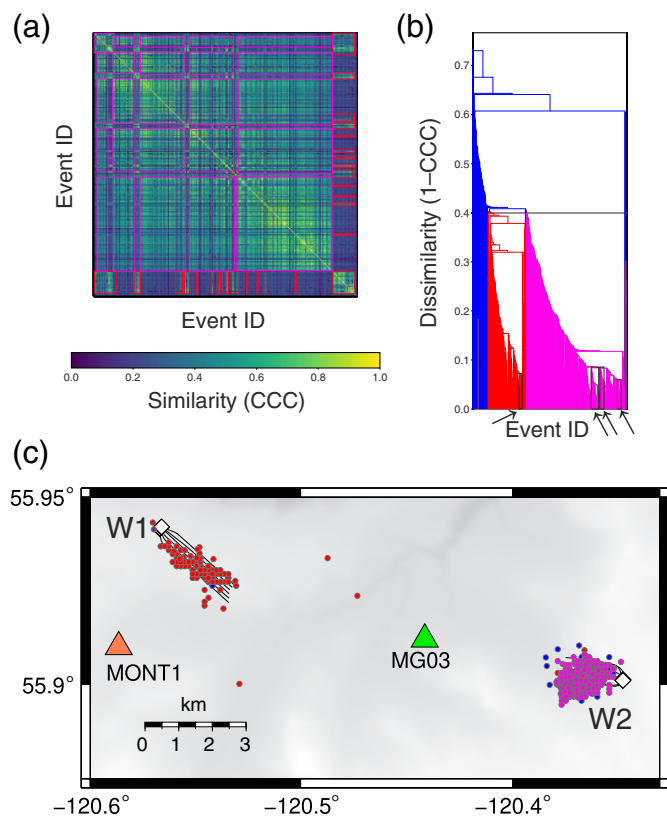
Figure 3. Waveform-similarity-based clustering for the time window of 27 March 2019–13 April 2019. (a) Network similarity matrix, in which each pixel indicates the cross-correlation coefficient (CCC) for the intersecting events (event pairs) indicated on the axes. Colorbar below indicates the CCC. (b) Dendrogram imaging the hierarchical clustering among the events shown in the similarity matrix in (a). We choose a threshold CCC > 0.6, or dissimilarity (1 − CCC) < 0.4 (indicated by the gray line) to define earthquake families, in which two families are defined in (b) (red and magenta branches), and a number of unassociated events are shown with blue branches. (c) Plot showing the initial catalog locations of the events within the time window, in which the color coding matches (b). Diamonds indicate the well head location of the active wells in the same period. The color version of this figure is available only in the electronic edition.

normally distributed, as they could be biased by station-dependent site effects. If the assumption of a normal distribution is violated, then estimating a mean, variance, or confidence intervals requires additional considerations. Thus, to obtain an approximate normal distribution of CCCs, we first combine the method with a Fisher transform before averaging the CCCs, followed by a reverse transformation before creating a dendogram of dissimilarity values, defined as 1 − CCC (We refer the reader to VanDecar and Crosson, 1990; Grund et al., 2016, for further details). The CCC approach has been applied extensively in the identification of HF-induced earthquakes, for example, among the first-reported HF-induced sequences near the Crooked Lake, Alberta

(Schultz, Stern, et al., 2015), and Ohio (Skoumal et al., 2015). Figure 3 shows an example of the network similarity matrix (Fig. 3a) and resulting dendrogram (Fig. 3b) from which we define event families (depicted in colors). Event families are defined by choosing the CCC (or dissimilarity 1 − CCC) threshold for which single-event branches are linked to an individual family branch, in this example CCC = 0.6. After defining the event family, we calculate its centroid epicentral location by taking the mean of all event latitude and longitude values from the initial earthquake catalog.

Given that the spatial event clustering is performed independently of temporal clustering in the matrix similarity approach, and that the temporal clustering was determined using an ad hoc approach (see the Earthquake Catalog Building section, Fig. 2), we check the consistency of the clustering results by applying the space–time–energy clustering as well. The second method is a statistical approach based on nearest-neighbor distances in a space–time–energy regime that simultaneously considers both temporal and spatial clustering. We follow the method described in Zaliapin et al. (2008), which is based on the time–space–magnitude distance between two earthquakes. Using the nearest-neighbor distances (i.e., the smallest distance of one earthquake to any other earthquake among the complete catalog), we divide our catalog in clusters or families, consisting of foreshocks, mainshocks, and aftershocks. The distribution of the nearest-neighbor distance is usually bimodal, with the mode characterized by larger rescaled times and distances representing the background Poissonian-like seismicity, and the short-proximity mode representing the clustered seismicity (i.e., foreshocks and aftershocks). In a region with low deformation rates and in the context of induced seismicity, such as the Dawson-Septimus area, background seismicity is mostly considered as being fluid driven. In contrast, clustered seismicity is commonly interpreted as the result of earthquake interactions (Zaliapin and Ben-Zion, 2016).

Both the waveform similarity approach and the space–time–energy clustering approach yield similar results, namely, that the seismicity occurs in tight spatial clusters around wells, and in close temporal association with HF stimulation. The space–time–energy clustering reveals a moderately unimodal distribution that does not unambiguously imply events mainly classified as background seismicity (see Fig. S3). Here, we reshuffle the catalog to identify the threshold between background seismicity and clustered events (see Fig. S4). We found that 64% of events are triggered by fluid injection (i.e., background seismicity) and 36% of events follow an earthquake–earthquake interaction pattern (clustered seismicity), which also supports the fact that earthquakes in the Dawson-Septimus area are dominated by spatial clusters related to injection activity (e.g., Zaliapin and Ben-Zion, 2016) instead of foreshock–mainshock–aftershock sequences. This is in agreement with the close hypocentral distribution around wells

inferred from the waveform similarity suggested by the CCCs. The waveform similarity approach has the added advantage of removing any false detections that were missed by the analyst, and/or detected events that occurred outside the study area that were erroneously located there with poor depth constraints. Thus, because it quantitatively describes the spatial clustering in this data set, and is able to remove events not related to HF stimulation, we prefer the cross-correlation-based waveform similarity method for classifying event families for the cluster-based double-difference relocation estimation. The clustering results for the entire catalog result in a total of 38 event families (Table S2) active within the 22 time windows indicated by gray-shaded areas in Figure 2.

Because of the short (<5 km) length scales of spatial clustering and capability to sort out regional events and/or false detections provided by waveform similarity, we use the matrix similarity clustering method to investigate the correlation between well stimulation and earthquake occurrence. In general, a small number of individual wells were active and spatially correlated with various groups of earthquake families active within the time windows bounded by gray areas (and the five-day buffer) in Figure 2. We plot the cumulative per-well-head HF stimulation activity within a spatial radius of 5 km from all active groups of clustered event families (considering the distance from the group centroids) within the specified windows (turquoise lines in Fig. 2). We note that turquoise lines within the gray time blocks indicate different operational wells between successive time blocks (Fig. 2). Considered in aggregate, the turquoise lines effectively represent spatial constraints on the influence of HF stimulation at individual wells (<5 km), whereas the gray-shaded areas encompass temporal windows in which event families proximal to the active wells occurred.

Figure 3 demonstrates the results for the temporal window 22 (27 March 2019–13 April 2019, Fig. 2), which is generally representative of the behavior observed in other temporal windows. The network similarity matrix in Figure 3a and the respective dendrogram in Figure 3b identify two event families and a number of unassociated events active in the time period. The bright colors in the similarity matrix (Fig. 3a) denote high CCCs for a given event pair represented as an individual pixel in the matrix, in which a pair can be identified by the two event IDs indicated on the axes. Events are sorted by time (earlier to later from right to left and bottom to top) in the similarity matrix and by CCC in the dendrogram (Fig. 3b). The dendrogram links all events with a CCC higher then 0.6 (i.e., a dissimilarity of 0.4) to individual event families (horizontal gray line in Fig. 3b). Associating all events with dissimilarity value of <0.4 to their respective branch defines two distinct event families (shown in red and magenta) in which individual events not associated within a family are shown by the blue branches. Figure 3c shows the initial catalog locations of the two event families observed in the time window indicated earlier (as well

as the nonassociated, dissimilar events in the dendrogram) and the location of the two active wells. Thus, the temporal correlation shows two active wells, each with their respective event groups that are spatially correlated to them.
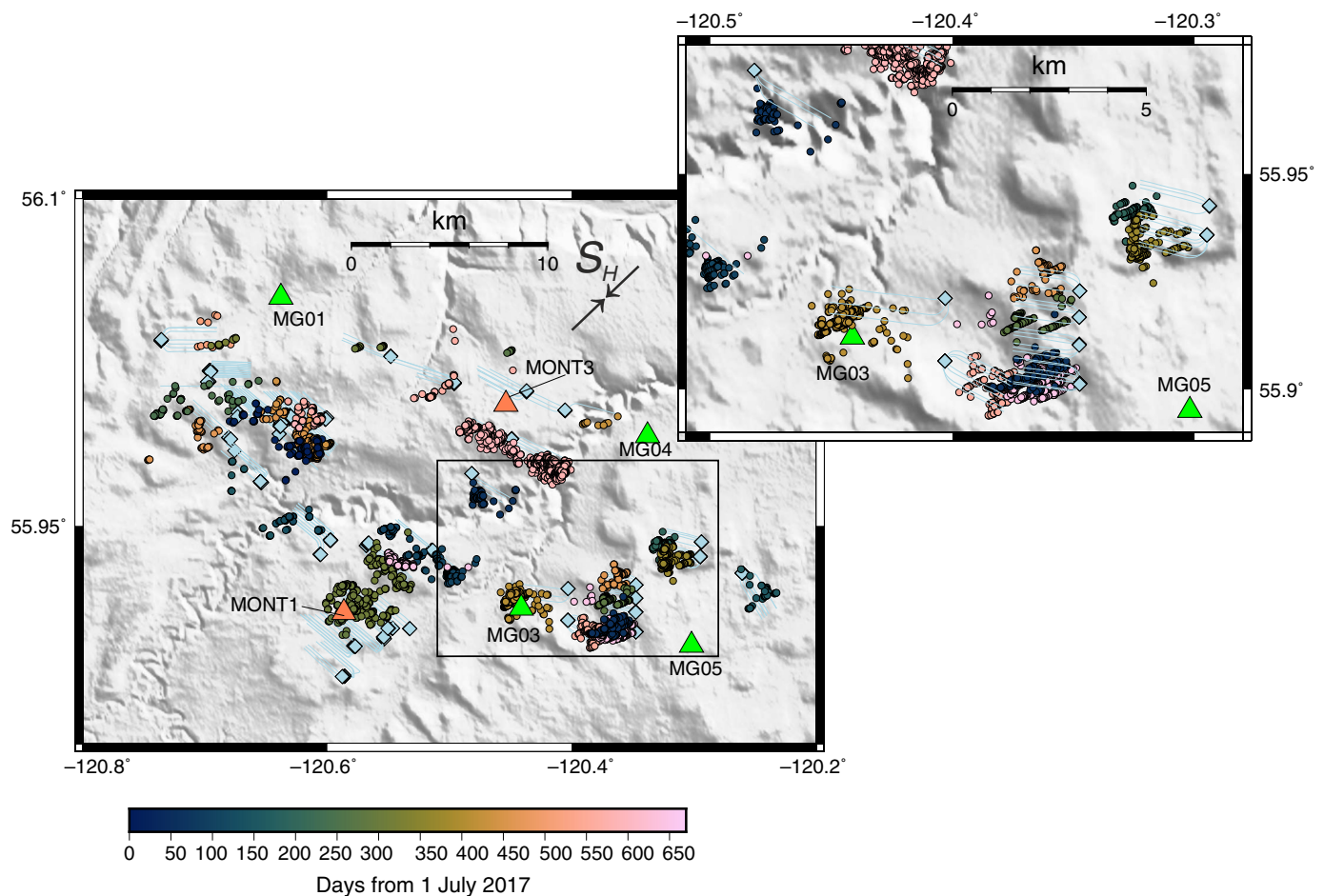
Seismicity Relocation

Initial event locations in the catalog described in the Earthquake Catalog Building section, used for clustering in the Event Spatiotemporal Clustering section, have horizontal errors on the order of several kilometers (albeit <3 km). As the expected length scale of events with magnitudes ranging between one and three (the majority of events) is in the range of several meters to 1 km (e.g., Wells and Coppersmith, 1994; Bohnhoff et al., 2009), the initial locations do not permit interpretation of activated geological structures. We applied the cross-correlation-based clustering on the 4883 events with a horizontal error <3 km and found 526 events, which are either false detections, erroneously located events, or events that do not exceed the CCC threshold. Therefore, we removed the 526 events before calculating relative relocations. Figure 4 shows the relocated epicenters estimated in clustering mode based on families. The relocation settings summarized above led to 4191 relocations of the of the 4883 earthquakes from the initial catalog (Fig. 4) with horizontal relative location errors of 13 ± 28 m and vertical relative location errors of 29 ± 59 m. The hypocentral depth distribution of the relocated events suggests that most earthquakes occurred slightly above the injection horizons (ranging from 2 to 2.4 km), at depth ranges between 1.75 and 2 km (Fig. 5).

Given that the earthquake clusters around wells form distinct event families with similar waveforms that are largely spatially separated from neighboring families, it suggests that they occur on individual or related systems of geological structures and are suited to a cluster-based approach to double-difference relocation. We therefore refine the initial locations in attempts to image the geological structures and their orientations that are activated during stimulation periods.

We use HypoDD v.1.3 to calculate double-difference relative relocations within event clusters determined from the matrix similarity approach following the method described in Waldhauser and Ellsworth (2000). The double-difference algorithm minimizes residuals between observed and calculated travel-time differences between one event pair recorded on a common station in an iterative fashion using a least-squares method. As HypoDD more effectively constrains relative, as opposed to absolute, locations, we perform relative relocations of individual event per family, while keeping family cluster centroids fixed by the initial cluster locations. We use stations within a distance threshold of 100 km of cluster centroids, where station information is listed in Table S1.

Double-difference relocations within event families were estimated using differential arrival times measured from cross-correlation lag times of individual earthquake waveforms

Figure 4. Full-scale map of 4191 double-difference event relocations. Color code, network, and HF wells are consistent with Figure 1. Inset map highlights the details of lineations in seismicity revealed by the clustered relocation approach, which includes east-northeast- and northwest-trending lineations. The east-northeast lineations are narrow, suggesting near-vertical-dipping faults, whereas more diffuse northwest lineations suggest fault structures with shallower dip angles (relative to vertical). The color version of this figure is available only in the electronic edition.

recorded on a given station. The cross-correlation time shift calculation uses 2.5 s time windows starting 1 s before and 1.5 s after the phase arrival picks, which are band-pass-filtered between 2 and 15 Hz. We use differential travel-time picks in which the CCC exceeds 0.6 in the cluster relocation. As our initial locations have a horizontal error less than 3 km, we weight the cataloged arrival times more heavily than cross-correlation differential times for the first five iterations by a ratio of 1/100. We then weight the cross-correlation travel times by a ratio of 100/1 relative to the absolute phase picks for the subsequent 20 iterations to effectively use the waveform similarity to reduced relative location errors. CCC values between event pairs determine the waiting for relative travel times, for which catalog phase arrival picks are set using an SNR-based weighting. For event families with less than 20 earthquakes, we use singular value decomposition to minimize residuals, and the conjugate gradients method (Paige and Saunders, 1982) for larger numbers of events.

Figure 6a,b shows the earthquake relocation results based on the similarity matrix cluster classification in Figure 3b for the two event families in the time window. Individual lineations among one event family in Figure 6 are highlighted by the arrows in Figure 3b, which show even higher common CCCs for a small number of events in one event family. The relative relocations and the colorbar in the right of each panel in Figure 6

demonstrate the spatial and temporal proximity to HF stimulation operations and the well bore. Both panels show event families of seismicity occurring up to approximately two weeks after stimulation commences (also shown in Fig. 2).

Details of event relocations also reveal distinct migration patterns groups of families in close proximity to active wells as well. For example, Figure 7 shows one active family with a CCC > 0.7 grouped around the well labeled W3 that seems to progressively follow individual HF stages. Denoted with different symbols are events of this event family, which share an even higher common CCC > 0.82. Figure S6c shows similar migration behavior exhibited at other time periods in other locations as well.
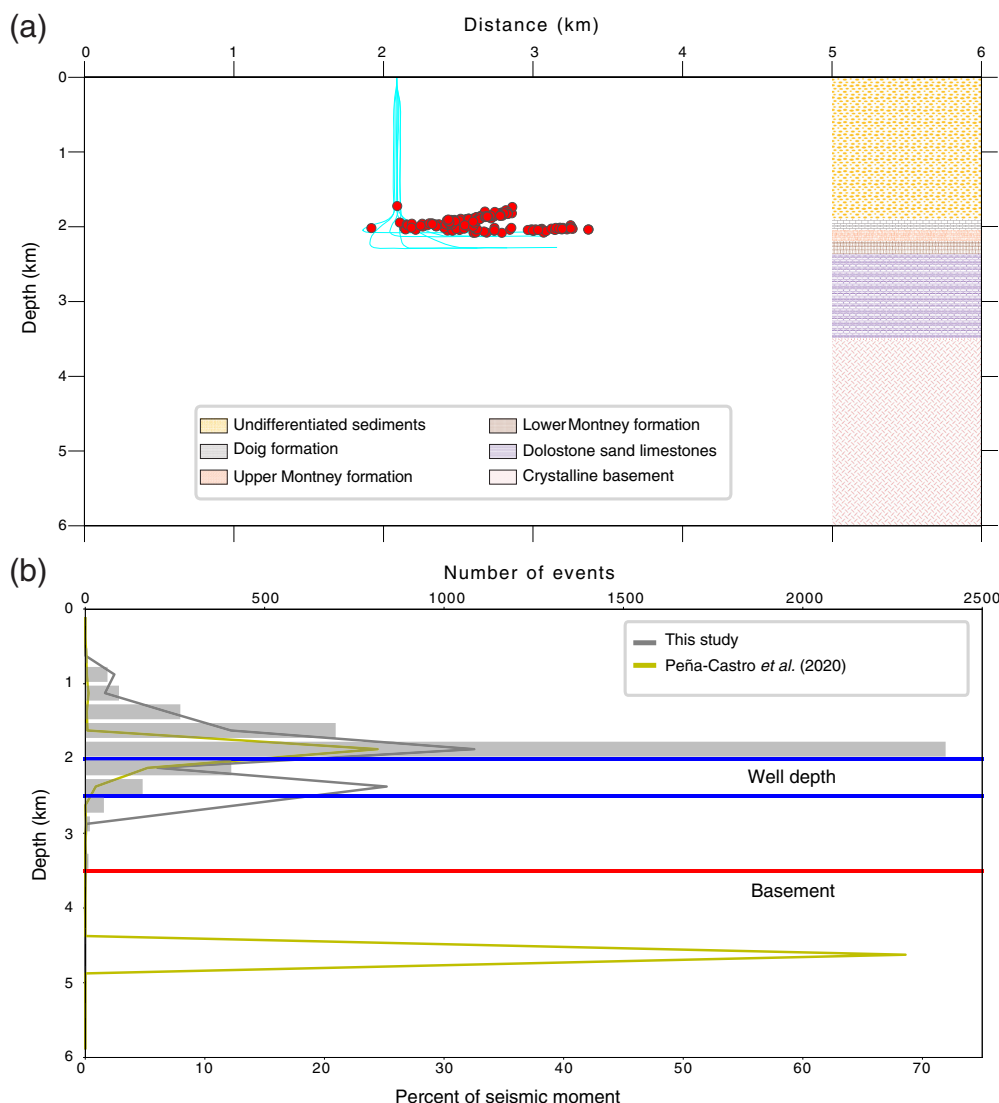
Figure 5. Example of depth distribution with respect to well location. (a) Depth cross section roughly parallel to S_H of the relocated hypocenters (red dots) from time window 19 (5–11 January 2019) with respect to the HWs in turquoise and geological units indicated. (b) Histogram of depth distribution of all relocated events, with horizontal lines indicating the well operation depths (blue, Upper and Lower Montney) and the boundary between sediment layers and crystalline basement (red). Colored curves show the percentage of cumulative seismic moment in 250 m depth intervals from the relocated events in this study (gray) and the relocations from the November 2018 M_L 4.5 sequence, 20 November 2018 to 10 December 2018, by Peña-Castro et al. (2020) (yellow). The difference in hypocentral depths for the M_L 4.5 earthquake (corresponding to the jump in cumulative moment at 4.5 km depth) results from a larger number of events from a matched-filter enhanced catalog in the study of Peña-Castro et al. (2020). The color version of this figure is available only in the electronic edition.

from an individual well pad, shown in detail for a single shaded time period in Figure 8 (corresponding to area 19, outlined in Fig. 2). Figure 8a shows seven horizontal well (HW) trajectories color coded using the same scheme as the temporal injection history in Figure 8b, which also includes information on the volume per stimulation phase. The color-bar below Figure 8a shows the time progression of earthquakes since the first cluster, associated with HW 35845 in Figure 8b and northeast part in Figure 8a, highlighted by the blue oval. In particular, Figure 8b shows that even in a one-week time window, when multiple HWs from the same well pad are stimulated (outlined in Fig. 2), the majority of earthquakes occurred during the active stimulation periods. In fact, 163 out of the 202 events shown in Figure 8 occurred during ongoing stimulation, that is, roughly 81%. In addition, most of the earthquakes seem to occur associated with stimulation at primarily 3/7 of the HWs, which do not necessarily correspond to the three highest per-stage injection volumes. Schultz and Wang (2020) observed similar behavior in which events occurred more commonly during stimulation periods in the Duvernay east shale basin, approximately 700 km to the southeast of our study area, near Red Deer, Alberta.

Discussion

The earthquake catalog and temporal progression of events illustrated in Figures 1 and 2 show strong temporal and spatial clustering for earthquakes in the Dawson-Septimus area, with comparatively low levels of background activity outside of hydraulic stimulation periods. The strong temporal and spatial clustering is also evident at the scale of multistage stimulation

The matrix similarity clustering considered together with the location of active wells in the time windows of heightened activity provides a correlation between the occurrence of earthquakes and HF operations that suggest the majority of events can be attributed to HF-driven fluid injection. The number of events not associated with event families defined by the matrix similarity clustering and/or occurring outside of time periods
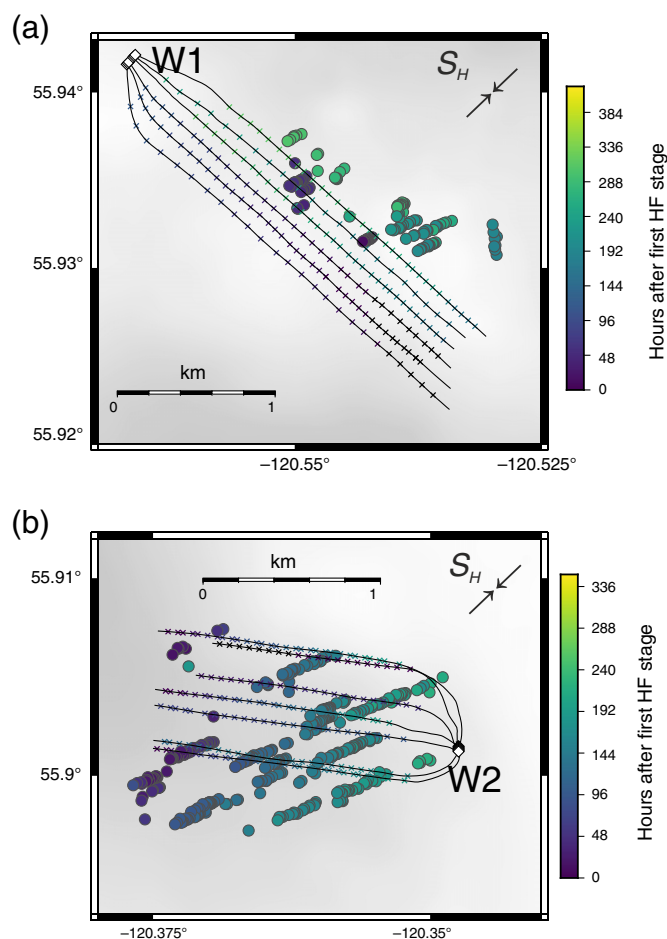
(a)

(b)

Figure 6. Relative relocations of the (a) red and (b) magenta event families shown in Figure 3 in the 22nd time window. The colorbar shows the temporal migration of events (circles) and HF stages (crosses along HW trajectories) in hours following the first HF stage. Relocations show strong lineations trending east-north-east at low angles to S_H. The color version of this figure is available only in the electronic edition.

Figure 7. Relative relocations of the event family in time window 21, defined with similarity >0.7. The colorbar shows the temporal migration of events (circles) and HF stages (crosses along HW trajectories) in hours following the first HF stage. Each symbol group indicates a subfamily with an even higher similarity (≥0.82) than the whole-family threshold. In addition to the temporal migration, relocations show the same strong lineation as in Figure 6. See Figure S5 for initial locations. The color version of this figure is available only in the electronic edition.

of heightened activity is generally low compared with families temporally and spatially associated with stimulation at individual wells, which also supports the idea of the majority of events being induced seismicity. Our interpretation is consistent with observations from Schultz, Stern, et al. (2015) in which the CCC-identified seismicity of the 2013–2014 Crooked Lake sequences have more than 99% temporal correlation with the HF operations in the Duvernay Formation in Alberta. Similar results are reported by Skoumal et al. (2015), who saw a swarmlike behavior of seismicity within a radius of 5 km of fluid injection activity in Ohio using a CCC-based detection method. Moreover, Schaff and Waldhauser (2005) demonstrated a decrease of CCC between 0.15 and 0.3, dependent on the confidence level of calculated CCCs, for events with interevent distances >1 km, suggesting that the waveform character differentiates significantly as the ray paths diverge. Their observations help us interpret CCC differences for events
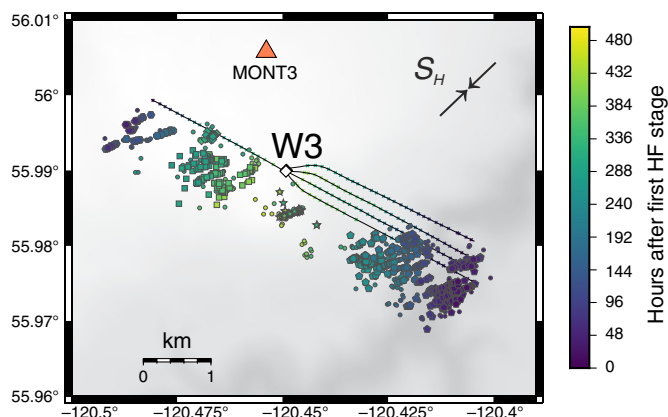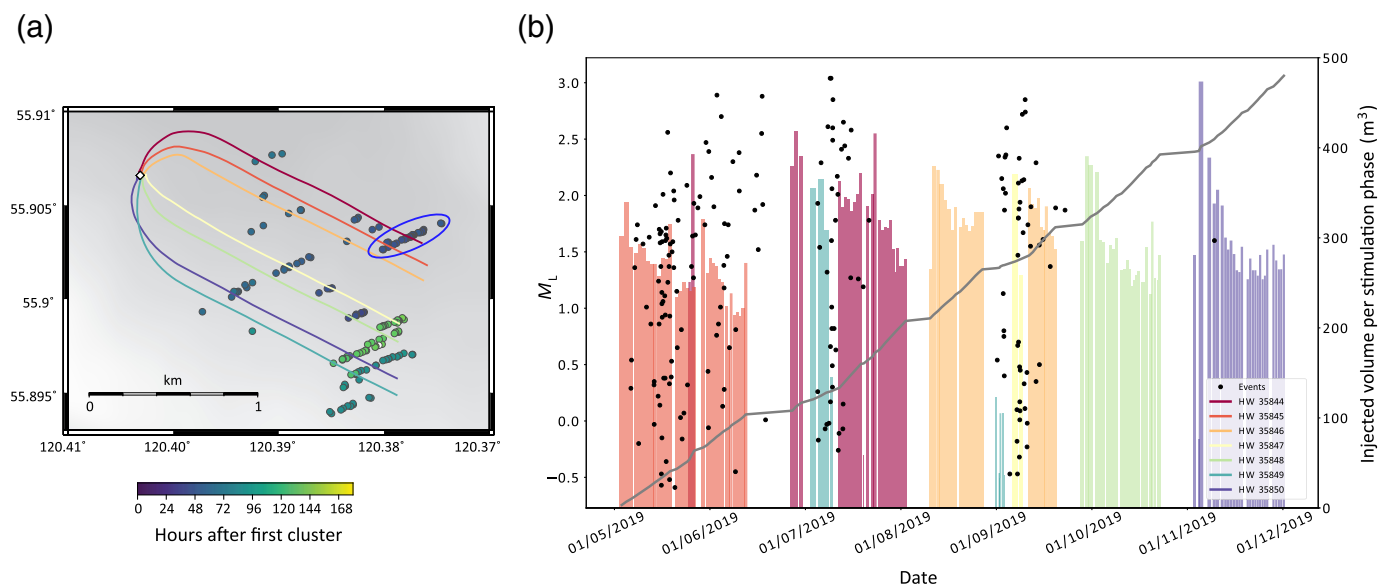
surrounding only one HF well as spatially separated event families, more precisely as individual fault structures (see Fig. 7 and Fig. S6). Furthermore, the statistical clustering approach performed as a consistency check to the matrix similarity clustering indicates a unimodal seismicity distribution (Fig. S3), interpreted by Zaliapin and Ben-Zion (2016) to suggest dominantly induced seismicity in spite of HF stimulation.

The fact that well stimulation temporally associated with earthquakes also occurs on such close spatial scales implies that increased pore pressure may be the driving mechanism for many of the events. Furthermore, pore-pressure increase has been interpreted as the primary driving force for HF-induced seismicity on a regional scale, including those in the Duvernay and Montney Formations. For example, Schultz et al. (2018) showed that for the Duvernay Formation, the event count increases with the injection volume, which supports the idea of pore-pressure increase being the dominant factor for earthquake occurrence as opposed to the injection rate. In a related study, Shen et al. (2019) performed slip tendency simulations showing that measured pore-pressure perturbations in the Duvernay Formation near Fox Creek, Alberta, were significant enough to impact pore-fluid pressure on optimally oriented fault planes. The changes were significant enough to move potential slip planes into the unstable regime, thereby triggering larger magnitude events. In another example in the Montney Formation, Yu et al. (2019) also observed clustered seismicity within 5 km of the active well bore and found pore pressure to dominate over poroelastic stresses at such short distances. Their interpretation was also based on HF injection data and poroelastic modeling in which parameter choice was based

Figure 8. Detailed view of the spatiotemporal correlation between seismicity and well stimulation during the time period indicated by the gray-shaded area outlined in Figure 2. (a) Relative relocations of 202 events. The colorbar shows the temporal migration of events since the first cluster in this sequence, marked by the blue oval (northeast part of the plot). Colored lines represent the different horizontal wells (HWs) color coded according to (b). (b) Temporal evolution of injection at individual wells (color coded histogram) and seismicity (shown as circles in (a)) corresponding to 202 events. A fraction of 81% (163/202) of the earthquakes occur during an ongoing well stimulation. Colored bars show the injected fluid volume per stimulation phase for each HW, and the gray line shows the relative fraction of cumulative injected volume. The color version of this figure is available only in the electronic edition.

on estimated diffusivity values of $D = 0.2$ m^2 s^{-1} inferred via migration patterns at a nearby site to the north in the Montney Formation. In addition, Yu *et al.* (2019) inferred a negligible effect of pore-pressure perturbation on induced events at distances greater than 5 km to the well bore. Our spatial and temporal distribution of events mimics the observations in Yu *et al.* (2019) and suggests that, at least within 5 km of the well bore, pore-pressure perturbations may dominate over poroelastic stresses in triggering many of the identified clusters.

In addition to the clear spatial correlation of seismicity with HWs in the map view as discussed previously, the relocated hypocenters are also closely associated with the well trajectories in the depth distribution. The results presented here show a predominantly shallow clustering of events primarily above the HWs for individual stimulation periods (Fig. 5a), as well as for the complete relocated catalog (Fig. 5b). The depth distribution is consistent with observations of shallow hypocentral depths above or around individual HWs of induced seismicity in the WCSB, including multiple compartments of the Duvernay Formation in Alberta (e.g., Schultz *et al.*, 2017; Eaton *et al.*, 2018; Schultz and Wang, 2020). Although the seismic moment release is located entirely in the sedimentary layers based on the full catalog relocation in this study (gray line in Fig. 5b), we note that in a detailed source parameter study of the 30 November 2018 M_L 4.5 sequence (Peña-Castro *et al.*, 2020) the 4.5 mainshock is relocated at ∼4.5 km in the crystalline basement, as a result of better relocation constraint from a larger number of events in a matched-filter enhanced catalog. The M_L 4.5 accounts for nearly 70% of the total seismic moment in the basement, despite the overwhelming number of events in the sedimentary layers. Such disparity in the distributions of event number and seismic moment proportion has also been reported for relatively larger magnitude events in the Duvernay Formation (Bao and Eaton, 2016).

Although spatial and temporal clustering is consistent with pore pressure generating induced events, the distribution of relocated hypocenters, their observed temporal migration, and the orientation of the regional stress field suggest that natural, preexisting fault surfaces are being activated by HF injection activity. Figures 4, 6, and 7 all show lineations in the seismicity distribution trending east-northeast (60°), where many lineations define clear lines suggesting near-vertical faults often associated with transverse fault motion. According to the ambient stress field, that is, $S_H = 43.7° \pm 7.3°$ and $S_H > S_h > S_v$ (Bell and Grasby, 2012), thrust faulting perpendicular to S_H would be the preferred rupture mechanism. Relative relocations also suggest another dominant alignment direction to the east-northeast direction, namely an additional one striking southeast, roughly parallel to the direction of S_h and the HW trajectories (Fig. 1). The slip surfaces implied by the lineations oriented roughly 30° from S_H would suggest a principle stress field in which $S_H > S_v > S_h$ and strike-slip faulting (Anderson, 1951). Both thrust and strike-slip deformation might be expected where local variations in pore

pressure perturb the balance between $S_v > S_h$ disproportionately, and/or where they are close in magnitude. In either case, the lineations apparent in the relative earthquake relocations (east-northeast or southeast) are consistent with optimally oriented faults in the regional stress field. Thus, the distribution of relocated hypocenters is consistent with activation (or reactivation) of pre-existing structures, rather than mode I type fracturing directly related to the hydrofracture process.

Focal mechanism solutions of earthquakes from additional studies in the WCSB (M_w 3+ events outside the study area of this work and M_w 1.8+ events in Peña-Castro, Peña-Castro et al., 2020). Eaton and Babaie Mahani (2015), Schultz, Mei, et al. (2015), Wang et al. (2016, 2018), Zhang et al. (2016), Babaie Mahani et al. (2017, 2020), Schultz et al. (2017), Onwuemeka et al. (2019), and Peña-Castro et al. (2020) offer further support for the above interpretation of (re)activated pre-existing structures, as well as the distribution of relocated hypocenters on both thrust and strike-slip faults. Figure 1b demonstrates consistent results with those presented here and discussed earlier, namely thrust-faulting mechanisms with fault strike oriented roughly to the southeast, perpendicular to S_H, and transform faults striking dominantly at low angles to S_H, that is, striking east-northeast in our study area and adjacent regions in western Alberta. Furthermore, in a comparison of two differing types of focal mechanism solutions commonly observed in the WCSB, a seismic anisotropy study (Li et al., 2019) supports a model of branched faults and fractures surrounding induced earthquakes near Fox Creek, Alberta, which may also explain the varying alignments of seismicity imaged in this study. Thus, their results and the results of this study highlight two major seismotectonic features: (1) an activated thrust-fault belt in the Rocky Mountains foreland (Paná and van der Pluijm, 2015) and (2) normal faults that formed related to synchronous graben building and basin infill (e.g., Barclay et al., 1990; Davies, 1997), which could become reactivated as thrust faults in the current stress field. In contrast, the localized east-northeast-striking lineations of seismicity observed in Figure 4 might represent activation of more recently formed fault networks or the growth of pre-existing structural weaknesses, that have become activated as local stress conditions change with ubiquitous well stimulation (Reches and Lockner, 1994). The fact that most seismicity occurs slightly above the injection horizon (Fig. 5) lends additional support to the interpretation.

Finally, the fault orientations imaged by relative relocations and the progressive migration of seismicity along the well bore with progressive stage stimulation suggests that although injection provides the "push" that initiates fault slip, the structures activated are governed by regional stress and earthquake–earthquake interaction as also suggested by the space–time–energy clustering approach. Figure 7 shows additional east–northeast-trending structures progressively activated at both ends of the well bores, where stimulation starts, and migrates over the stimulation period closer to the well pad (as distal stages are injected into first, and stages progressively closer to the well pad are stimulated afterward). Locally, S_h is roughly parallel to the well bore, suggesting that hydrofractures should form at right angles, that is, in the direction of S_H. Of course one should keep in mind absolute error in event location that is on the order of kilometers; however, the relative location within the family clusters is smaller than the stage spacing, which is on the order of 100 m. Thus, it is hard to relate which events are related to which stage, but the relative progression between events and stimulation stages is consistent, suggesting that the observed migration pattern does indeed track the stage progression, and that individual lineations activated within hours may represent the activation of structures optimally oriented with relation to S_H.

Conclusions

Here, we present a new, detailed earthquake catalog for the Dawson-Septimus area in the Montney Formation, British Columbia, in a time period from 1 July 2017 to 30 April 2019. It provides the first detailed look at HF-induced events detected and located using a new data set of 15 broadband stations in this area. We detected 5757 local earthquakes in total during the study period, of which 4883 have a horizontal location error smaller then 3 km. A maximum-likelihood estimate suggests a catalog completeness of $M_c = 1.3$, and a Gutenberg–Richter b-value of 0.92.

Clustering analysis reveals 22 time windows of elevated seismicity, in which 38 event families and a small proportion of unassociated events were active, and in which background seismicity levels outside of the time periods was low. HF injection is temporally and spatially correlated with earthquake activity (within 5 km), where the close proximity to HF wells suggests earthquakes are triggered or induced mainly by pore-pressure diffusion. Double-difference event relocations show seismicity lineations both perpendicular to S_H and at low angles to S_H, consistent with the thrust and strike-slip deformation on optimally oriented faults in the ambient stress field. Thrust-fault motion would be consistent with either reactivated normal faults in the Fort St. John graben complex or on faults of the Rocky Mountains thrust-fault belt. We interpret events with a strike-slip faulting mechanism to result from the activation of younger faults or crustal weaknesses activated by HF activity and controlled by regional stresses.

Data and Resources

Plots containing maps were made using the Generic Mapping Tools v.5.4.3 (www.soest.hawaii.edu/gmt, last accessed July 2018; Wessel et al., 2013), whereas the remaining figures were made using Matplotlib (Hunter, 2007). Color maps in Figures 1a and 4 are provided by Crameri (2018). Well data are provided by British Columbia Oil and Gas Commission (BCOGC; https://files.bcogc.ca/thinclient/, last accessed February 2020). The database was last accessed in February 2020 and may potentially be updated in the time period following the submission of the article. Seismograms used in this study are part

of the Geological Survey of Canada (GSC)-BCOGC Induced Seismicity Study and Canadian National Seismograph Network were collected by McGill University and the Ruhr University Bochum (RUB) and are archived on the Incorporated Research Institutions for Seismology (IRIS) Data Management Center under network code XL (www.iris.edu, last accessed February 2020). Topographic information comes from http://srtm.csi.cgiar.org (last accessed October 2018; Jarvis *et al.*, 2008), and shapes of the Montney Formation in Figure 1a inset map are obtained by BCOGC (https://data-bcogc.opendata.arcgis.com/, last accessed October 2018) and Alberta Energy Regulator (https://www.aer.ca, last accessed May 2020). We used primarily the ObsPy toolbox for data processing (https://github.com/obspy/obspy/wiki, last accessed February 2020 [version 1.2.1]; Beyreuther *et al.*, 2010). The supplemental material of this article provides station location and operation periods, the velocity model, the frequency–magnitude distribution, event family centroids and number of events, results from the nearest-neighbor clustering, and further clustering and relocation examples.

Acknowledgments

References

Aki, K. (1965). Maximum likelihood estimate of b in the formula $\log n = a - bm$ and its confidence limits, *Bull. Earthq. Res. Inst. Tokyo* **43**, 237–239.

Anderson, E. M. (1951). *The Dynamics of Faulting and Dyke Formation with Applications to Britain*, Hafner Pub. Co, Oliver and Boyd, London, United Kingdom.

Atkinson, G. M., D. W. Eaton, H. Ghofrani, D. Walker, B. Cheadle, R. Schultz, R. Shcherbakov, K. Tiampo, J. Gu, R. M. Harrington, *et al.* (2016). Hydraulic fracturing and seismicity in the Western Canada Sedimentary Basin, *Seismol. Res. Lett.* **87**, no. 3, 631–647.

Babaie Mahani, A., F. Esfahani, H. Kao, M. Gaucher, M. Hayes, R. Visser, and S. Venables (2020). A systematic study of earthquake source mechanism and regional stress field in the southern Montney unconventional play of northeast British Columbia, Canada, *Seismol. Res. Lett.* **91**, no. 1, 195–206.

Babaie Mahani, A., H. Kao, G. M. Atkinson, K. Assatourians, K. Addo, and Y. Liu (2019). Ground-motion characteristics of the 30 November 2018 injection-induced earthquake sequence in Northeast British Columbia, Canada, *Seismol. Res. Lett.* **90**, no. 4, 1457–1467.

Babaie Mahani, A., R. Schultz, H. Kao, D. Walker, J. Johnson, and C. Salas (2017). Fluid injection and seismic activity in the northern Montney play, British Columbia, Canada, with special reference to the 17 August 2015 M_w 4.6 induced earthquake, *Bull. Seismol. Soc. Am.* **107**, no. 2, 542–552.

Bao, X., and D. W. Eaton (2016). Fault activation by hydraulic fracturing in western Canada, *Science* **354**, no. 6318, 1406–1409.

Barclay, J., F. Krause, R. Campbell, and J. Utting (1990). Dynamic casting and growth faulting: Dawson Creek graben complex, Carboniferous-Permian Peace River embayment, western Canada, *Bull. Can. Petrol. Geol.* **38**, no. 1, 115–145.

British Columbia Oil and Gas Commission (BCOGC) (2017). British Columbia's Oil and Gas Reserves and production report, available at https://www.bcogc.ca/publications/reports (last accessed September 2019).

Bell, J., and S. Grasby (2012). The stress regime of the Western Canadian Sedimentary Basin, *Geofluids* **12**, no. 2, 150–165.

Beyreuther, M., R. Barsch, L. Krischer, T. Megies, Y. Behr, and J. Wassermann (2010). ObsPy: A python toolbox for seismology, *Seismol. Res. Lett.* **81**, no. 3, 530–533.

Bohnhoff, M., G. Dresen, W. L. Ellsworth, and H. Ito (2009). Passive seismic monitoring of natural and induced earthquakes: Case studies, future directions and socio-economic relevance, in *New Frontiers in Integrated Solid Earth Sciences*, Springer, 261–285.

Crameri, F. (2018). Scientific colour-maps, *Zenodo*, doi: 10.5281/zenodo.1243862.

Davies, G. R. (1997). The triassic of the Western Canada Sedimentary Basin: Tectonic and stratigraphic framework, paleogeography, paleoclimate and biota, *Bull. Can. Petrol. Geol.* **45**, no. 4, 434–460.

Eaton, D. W., and A. Babaie Mahani (2015). Focal mechanisms of some inferred induced earthquakes in Alberta, Canada, *Seismol. Res. Lett.* **86**, no. 4, 1078–1085.

Eaton, D. W., N. Igonin, A. Poulin, R. Weir, H. Zhang, S. Pellegrino, and G. Rodriguez (2018). Induced seismicity characterization during hydraulic-fracture monitoring with a shallow-wellbore geophone array and broadband sensors, *Seismol. Res. Lett.* **89**, no. 5, 1641–1651.

Ellsworth, W. L. (2013). Injection-induced earthquakes, *Science* **341**, no. 6142, 1225942.

Ghofrani, H., G. M. Atkinson, R. Schultz, and K. Assatourians (2019). Short-term hindcasts of seismic hazard in the Western Canada Sedimentary Basin caused by induced and natural earthquakes, *Seismol. Res. Lett.* **90**, no. 3, 1420–1435.

Grund, M., J. C. Groos, and J. R. Ritter (2016). Fault reactivation analysis using microearthquake clustering based on signal-to-noise weighted waveform similarity, *Pure Appl. Geophys.* **173**, no. 7, 2325–2355.

Hunter, J. D. (2007). Matplotlib: A 2D graphics environment, *Comput. Sci. Eng.* **9**, no. 3, 90–95.

Jarvis, A., H. Reuter, A. Nelson, and E. Guevara (2008). Hole-filled seamless SRTM data V4: International Centre for Tropical Agriculture (CIAT), available at http://srtm.csi.cgiar.org (last accessed October 2018).

Laske, G., G. Masters, Z. Ma, and M. Pasyanos (2013). Update on CRUST1.0—A 1-degree global model of Earth's crust, *Geophys. Res. Abstr.* **15**, 2658.

Lei, X., D. Huang, J. Su, G. Jiang, X. Wang, H. Wang, X. Guo, and H. Fu (2017). Fault reactivation and earthquakes with magnitudes of

up to M_w 4.7 induced by shale-gas hydraulic fracturing in Sichuan Basin, China, *Sci. Rep.* **7,** no. 1, 7971.

Lei, X., Z. Wang, and J. Su (2019). The December 2018 M_L 5.7 and January 2019 M_L 5.3 earthquakes in South Sichuan Basin induced by shale gas hydraulic fracturing, *Seismol. Res. Lett.* **90,** no. 3, 1099–1110.

Li, T., Y. J. Gu, Z. Wang, R. Wang, Y. Chen, T.-R. A. Song, and R. Wang (2019). Spatiotemporal variations in crustal seismic anisotropy surrounding induced earthquakes near Fox Creek, Alberta, *Geophys. Res. Lett.* **46,** no. 10, 5180–5189.

Lomax, A., J. Virieux, P. Volant, and C. Berge-Thierry (2000). Probabilistic earthquake location in 3D and layered models, in *Advances in Seismic Event Location*, Springer, 101–134.

McGarr, A., B. Bekins, N. Burkardt, J. Dewey, P. Earle, W. Ellsworth, S. Ge, S. Hickman, A. Holland, E. Majer, *et al.* (2015). Coping with earthquakes induced by fluid injection, *Science* **347,** no. 6224, 830–831.

Onwuemeka, J., R. Harrington, Y. Liu, and H. Kao (2019). Source properties of earthquakes around hydraulic-fracturing sites near Dawson Creek, Northeastern British Columbia, *Geoscience BC Summary of Activities 2018: Energy and Water, Geoscience BC, Report 2019(2)*, 63–66.

Paige, C. C., and M. A. Saunders (1982). Algorithm 583: LSQR: Sparse linear equations and least squares problems, *ACM Trans. Math. Software* **8,** no. 2, 195–209.

Panǎ, D. I., and B. A. van der Pluijm (2015). Orogenic pulses in the Alberta Rocky Mountains: Radiometric dating of major faults and comparison with the regional tectono-stratigraphic record, *Geol. Surv. Am. Bull.* **127,** nos. 3/4, 480–502.

Peña-Castro, A. F., M. P. Roth, A. Verdecchia, J. Onwuemeka, Y. Liu, R. M. Harrington, Y. Zhang, and H. Kao (2020). Stress chatter via fluid flow and fault slip in a hydraulic fracturing induced earthquake sequence in the Montney formation, British Columbia, *Geophys. Res. Lett.* doi: 10.1029/2020GL087254.

Reches, Z., and D. A. Lockner (1994). Nucleation and growth of faults in brittle rocks, *J. Geophys. Res.* **99,** no. B9, 18,159–18,173.

Schaff, D. P., and F. Waldhauser (2005). Waveform cross-correlation-based differential travel-time measurements at the Northern California Seismic Network, *Bull. Seismol. Soc. Am.* **95,** no. 6, 2446–2461.

Schultz, R., and R. Wang (2020). Newly emerging cases of hydraulic fracturing induced seismicity in the Duvernay East Shale Basin, *Tectonophysics* **779,** 228393.

Schultz, R., G. Atkinson, D. Eaton, Y. Gu, and H. Kao (2018). Hydraulic fracturing volume is associated with induced earthquake productivity in the Duvernay play, *Science* **359,** no. 6373, 304–308.

Schultz, R., S. Mei, D. Panǎ, V. Stern, Y. J. Gu, A. Kim, and D. Eaton (2015). The Cardston earthquake swarm and hydraulic fracturing of the Exshaw Formation (Alberta Bakken play), *Bull. Seismol. Soc. Am.* **105,** no. 6, 2871–2884.

Schultz, R., V. Stern, M. Novakovic, G. Atkinson, and Y. J. Gu (2015). Hydraulic fracturing and the Crooked Lake sequences: Insights gleaned from regional seismic networks, *Geophys. Res. Lett.* **42,** no. 8, 2750–2758.

Schultz, R., R. Wang, Y. J. Gu, K. Haug, and G. Atkinson (2017). A seismological overview of the induced earthquakes in the Duvernay play near Fox Creek, Alberta, *J. Geophys. Res.* **122,** no. 1, 492–505.

Shen, L. W., D. R. Schmitt, and R. Schultz (2019). Frictional stabilities on induced earthquake fault planes at Fox Creek, Alberta: A pore fluid pressure dilemma, *Geophys. Res. Lett.* **46,** no. 15, 8753–8762.

Skoumal, R. J., M. R. Brudzinski, and B. S. Currie (2015). Distinguishing induced seismicity from natural seismicity in Ohio: Demonstrating the utility of waveform template matching, *J. Geophys. Res.* **120,** no. 9, 6284–6296.

VanDecar, J. C., and R. S. Crosson (1990). Determination of teleseismic relative phase arrival times using multi-channel cross-correlation and least squares, *Bull. Seismol. Soc. Am.* **80,** no. 1, 150–169.

Waldhauser, F., and W. L. Ellsworth (2000). A double-difference earthquake location algorithm: Method and application to the northern Hayward fault, California, *Bull. Seismol. Soc. Am.* **90,** no. 6, 1353–1368.

Wang, B., R. M. Harrington, Y. Liu, H. Kao, and H. Yu (2020). A study on the largest hydraulic-fracturing-induced earthquake in Canada: Observations and static stress-drop estimation, *Bull. Seismol. Soc. Am.* 1–12, doi: 10.1785/0120190261.

Wang, R., Y. J. Gu, R. Schultz, and Y. Chen (2018). Faults and non-double-couple components for induced earthquakes, *Geophys. Res. Lett.* **45,** no. 17, 8966–8975.

Wang, R., Y. J. Gu, R. Schultz, A. Kim, and G. Atkinson (2016). Source analysis of a potential hydraulic-fracturing-induced earthquake near Fox Creek, Alberta, *Geophys. Res. Lett.* **43,** no. 2, 564–573.

Weber, B., J. Becker, W. Hanka, A. Heinloo, M. Hoffmann, T. Kraft, D. Pahlke, J. Reinhardt, J. Saul, and H. Thoms (2007). SeisComP3 —Automatic and interactive real time data processing, *Geophys. Res. Abstr.* **9,** 09219.

Wells, D. L., and K. J. Coppersmith (1994). New empirical relationships among magnitude, rupture length, rupture width, rupture area, and surface displacement, *Bull. Seismol. Soc. Am.* **84,** no. 4, 974–1002.

Wessel, P., W. H. Smith, R. Scharroo, J. Luis, and F. Wobbe (2013). Generic Mapping Tools: Improved version released, *Eos Trans. AGU* **94,** no. 45, 409–410.

Wiemer, S., and M. Wyss (2000). Minimum magnitude of completeness in earthquake catalogs: Examples from Alaska, the Western United States, and Japan, *Bull. Seismol. Soc. Am.* **90,** no. 4, 859.

Yenier, E. (2017). A local magnitude relation for earthquakes in the Western Canada Sedimentary Basin, *Bull. Seismol. Soc. Am.* **107,** no. 3, 1421–1431.

Yu, H., R. M. Harrington, Y. Liu, and B. Wang (2019). Induced seismicity driven by fluid diffusion revealed by a near-field hydraulic stimulation monitoring array in the Montney Basin, British Columbia, *J. Geophys. Res.* **124,** no. 5, 4694–4709.

Zaliapin, I., and Y. Ben-Zion (2016). Discriminating characteristics of tectonic and human-induced seismicity, *Bull. Seismol. Soc. Am.* **106,** no. 3, 846–859.

Zaliapin, I., A. Gabrielov, V. Keilis-Borok, and H. Wong (2008). Clustering analysis of seismicity and aftershock identification, *Phys. Rev. Lett.* **101,** no. 1, 018501.

Zhang, H., D. W. Eaton, G. Li, Y. Liu, and R. M. Harrington (2016). Discriminating induced seismicity from natural earthquakes using moment tensors and source spectra, *J. Geophys. Res.* **121,** no. 2, 972–993.